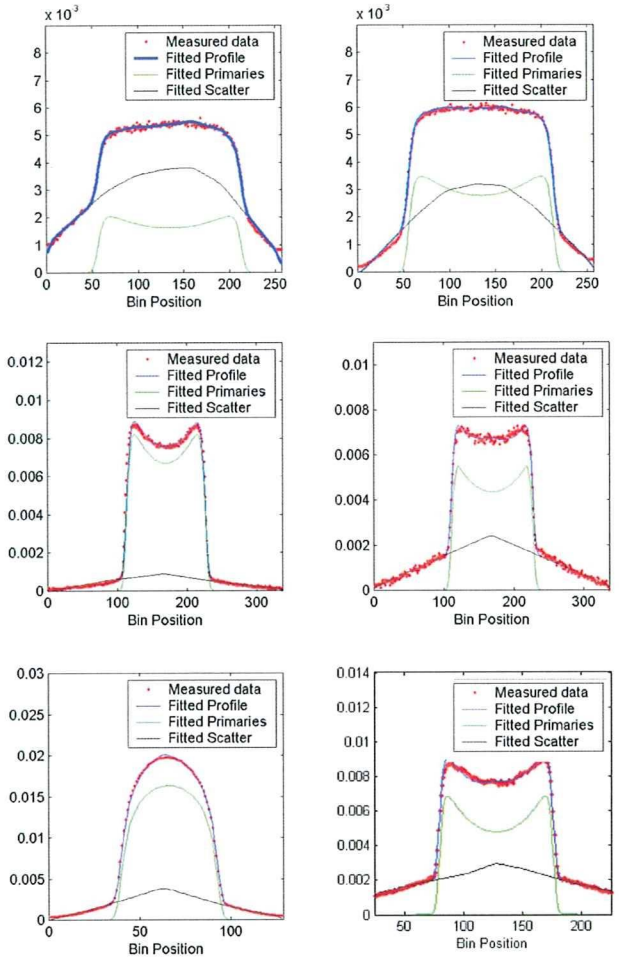

FIG. 4. Profiles of measured and fitted data. Top: HRRT before (left) and after (right) scanner setup. Mid: HR in 2D (left) and 3D (right) acquisition mode. Bottom: MicroPET (left) and Allegro (right). Due to the normalization process vertical units are arbitrary.

oblique planes (also called segment 1 and higher) were disregarded, effectively resulting in a 2D sinogram.

For the HRRT, SF-Daily was measured using a ^{68}Ge phantom (diameter of 20 cm, length of 27 cm, 20 MBq), routinely used for daily QC purposes. Sensitivity of SF-NEMA to small changes in SF was investigated by measuring SF of the HRRT just before and after performing a setup process (i.e., tuning of gain and other settings in order to maximize performance), as this setup process will decrease SF due to optimized energy calibration. SF was measured for the whole gantry and plane by plane. To assess effects of noise, SF-Daily for the whole gantry was measured using acquisition times of 15, 2, and 1 min.

For the Allegro, SF was determined for different lower energy threshold settings (260, 310, 360, and 410 keV) and an upper level discriminator set to 665 keV in order to investigate the correlation between both SF methods. For this a 20 cm diameter, 20 cm length cylinder filled with 20 MBq ^{18}F was used. As no mini-scatter-phantom was available for the microPET Focus 120, only SF-Daily was measured using a cylinder with an inner radius of 4.5 cm and a length of 10 cm, filled with 10 MBq, and this measurement was compared with published SF-NEMA values.[4]

TABLE II. Comparison of SF-NEMA and SF-Daily.

Scanner	SF-NEMA (%)	SF-Daily (%)
HRRT before setup	63	63
HRRT after setup	50	51
HRRT 15 min	50	51
HRRT 2 min	50	50
HRRT 1 min	50	50
HR 2D	14	13
HR 3D	38	33
MicroPET 45mm diameter cylinder	27[a]	23
Allegro	36	34

[a]The SF-NEMA was determined for a 60 mm phantom (8).

III. RESULTS

Sinogram profiles of the central axial plane and SF-Daily curve fits of total response $T(r)$ according to Eq. (1) are shown in Fig. 4 for all scanners. In addition, resulting primary $P(r)$ and scattered events $S(r)$ are shown. In all cases, the analytical response function equation (1) could be fitted to the data with high accuracy. Clearly, both shape and amplitude of the scatter distribution differ among scanners and acquisition modes. The HRRT setup process resulted in a lower SF and a more symmetric scatter distribution. Differences in scatter contribution between 2D and 3D modes are clearly illustrated by the HR profiles. The HR in 3D mode and the Allegro (measured using the lower level discriminator set at 410 keV) have similar profiles, indicating the impact of scanner geometry. The shape of the fitted primaries of the microPET deviates substantially from that of the other scanners due to the much smaller size of the phantom used. In general, SF measurement using SF-Daily were relatively insensitive to changes in PSF. Typically, doubling PSF (e.g., from 5 to 10 mm) resulted in only a 10% change in SF-Daily.

Table II summarizes SF values as obtained with SF-Daily and SF-NEMA. In addition, in case of the HRRT, SF values for different noise levels are included. Plane-by-plane SF values for the HRRT are shown in Fig. 5.

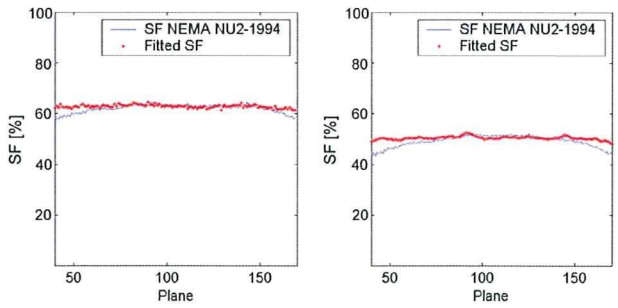

FIG. 5. Plane-by-plane values of SF-NEMA and SF-Daily (fitted SF) for the HRRT before (left) and after (right) setup.

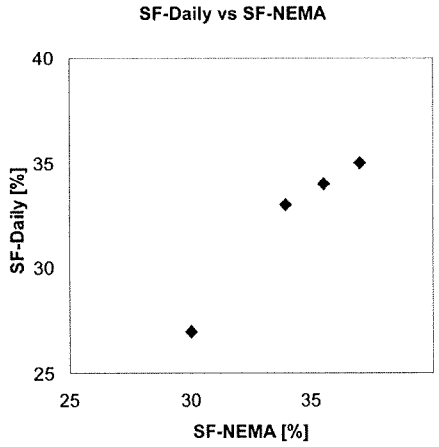

FIG. 6. SF-Daily and SF-NEMA values measured on the Allegro. Data points with higher SF refer to measurements with lower threshold values (260, 310, 360, and 410 keV).

Figure 6 shows SF values of the Philips Allegro for varying lower energy threshold settings. Both SF-NEMA and SF-Daily increased slightly with decreasing threshold channel, and a good correlation between both methods was found (R^2=0.96). Finally, Fig. 7 shows a Bland-Altman plot of the combined results presented in Table II and Fig. 6.

IV. DISCUSSION AND CONCLUSION

Using a simple curve fitting method, SF-Daily values were determined for different scanners and acquisition modes and compared to SF-NEMA values. A difference between SF-Daily and SF-NEMA only existed for the HR in 3D mode and for the microPET. For the latter, however, SF-Daily was measured using a cylinder with an inner diameter of 4.5 cm, while published SF-NEMA data were obtained with a cylinder of 6 cm diameter. The impact of noise was negligible for the three acquisition times investigated. The count rate in the HRRT scans was approximately 50 kcounts per slice, resulting in more than 100 counts per bin in the 1 min profiles, apparently sufficient for an accurate fit. The

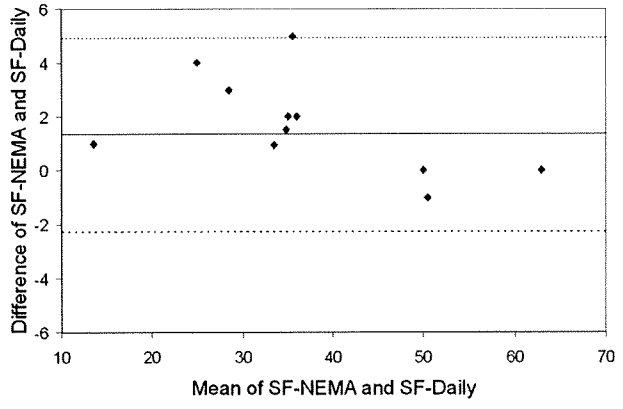

FIG. 7. Blant-Altman plot of all SF data from all four scanners and scan modes (data from Table II).

plane-by-plane comparison of SF-Daily and SF-NEMA showed good agreement especially in the center of the FOV. The slight deviation for the outer planes is probably due to the slightly longer phantom used for SF-NEMA than for SF-Daily.

In general, slight deviations in fitted and acquired profiles could be seen, especially at the maxima of the response (Fig. 4). Most likely these deviations are due to the fact that the thickness of the wall of the cylinder was not taken into account. Nevertheless, they have negligible effect on the resulting SF.

Similar to SF-NEMA, SF-Daily can be performed on either only a subset of the total sinogram, e.g., only on nonoblique (direct) planes, or on all sinogram planes/segments via a rebinning step.[5] The latter requires slight adaption of Eq. (1), as the primary response in oblique planes will be based on an oblique cross section of the phantom (in case of a cylinder this will become an ellipse) rather than a circle. In this study SF values were only determined using direct (2D) sinograms for both the SF-NEMA and SF-Daily methods. For one scanner these sinograms were derived from data acquired in both 2D mode (with septa) and 3D mode (without septa) in order to test different levels of scatter and randoms.

Although the SF-Daily method does require that the phantom is positioned in the center of the FOV, in practice it proved to be insensitive to slight misplacements. The method could, however, easily be extended with an algorithm to align the sinogram, similar to the SF-NEMA requirement.

One limitation is that not all scanners use cylindrical phantoms for daily QC purposes but rely on measurements of small sources in air. Although this has the benefit of requiring less activity, it gives the energy resolution at 511 keV rather than the scatter fraction. Furthermore, use of a point source in air also prohibits measurement of uniformity of coincidence timing over a large area of the FOV.

It should be emphasized that SF-Daily fits a profile to all projection data. This is in contrast to some scatter correction methods[17] that rely on fitting the tails of the scatter profile. In the presented approach all data are used and that knowledge about the primary response is included, making the method robust and insensitive to noise.

In general, SF-Daily values obtained were in close agreement with those derived using the NEMA protocol, making the method sufficiently sensitive to detect small changes in SF. Because the shape of the primary distribution is well known, accurate fits of the sum of scatter and primary events to the total profile can be achieved, without making prior assumptions about the shape of the scatter distribution. Furthermore no discontinuities in the estimated responses $S(r)$ were found. The method is also suitable for determining SF values in case of "dirty" radionuclides (i.e., radionuclides that emit gamma rays in addition to positrons),[18] activity outside the FOV, and phantoms with deviating dimensions, as long as the exact dimensions are known.

In conclusion, as this method does not require measurements with special phantoms, it can be used to accurately

monitor SF using both arbitrarily sized cylindrical phantoms and short acquisition times, making the method particularly useful for daily QC purposes.

[a]Author to whom correspondence should be addressed. Electronic mail: h.w.a.m.dejong@umcutrecht.nl; Telephone: +31-(0)88-7553327.

[1]G. Brix *et al.*, "Performance evaluation of a whole-body PET scanner using the NEMA protocol," J. Nucl. Med. **38**, 1614–1623 (1997).
[2]National Manufacturers Association, NEMA Standards Publication No. NU 2-1994 (National Manufacturers, Washington, DC, 1994).
[3]M. E. Daube-Witherspoon *et al.*, "PET performance measurements using the NEMA NU 2-2001 standard," J. Nucl. Med. **43**, 1398–1409 (2002).
[4]H. Herzog, L. Tellmann, C. Hocke, U. Pietrzyk, M. E. Casey, and T. Kuwert, "NEMA NU2-2001 guided performance evaluation of four Siemens ECAT PET scanners," IEEE Trans. Nucl. Sci. **51**, 2662–2669 (2004).
[5]National Manufacturers Association, NEMA Standards Publication No. NU 2-2001 (National Electrical Manufacturers, Washington, DC, 2001).
[6]National Manufacturers Association, NEMA Standards Publication No. NU 2-2007 (National Electrical Manufacturers, Washington, DC, 2007).
[7]E. J. Hoffman, S. C. Huang, M. E. Phelps, and D. E. Kuhl, "Quantitation in positron emission computed tomography: 4. Effect of accidental coincidences," J. Comput. Assist. Tomogr. **5**, 391–400 (1981).
[8]C. de Boor, *A Practical Guide to Splines* (Springer-Verlag, New York, 1978).
[9]D. Marquardt, "An algorithm for least-squares estimation of nonlinear parameters," SIAM J. Appl. Math. **11**, 431–441 (1963).
[10]C. C. Watson, M. E. Casey, L. Eriksson, T. Mulnix, D. Adams, and B. Bendriem, "NEMA NU 2 performance tests for scanners with intrinsic radioactivity," J. Nucl. Med. **45**, 822–826 (2004).
[11]H. W. de Jong, F. H. van Velden, R. W. Kloet, F. L. Buijs, R. Boellaard, and A. A. Lammertsma, "Performance evaluation of the ECAT HRRT: An LSO-LYSO double layer high resolution, high sensitivity scanner," Phys. Med. Biol. **52**, 1505–1526 (2007).
[12]K. Wienhard *et al.*, "The Ecat exact HR—Performance of a new high-resolution positron scanner," J. Comput. Assist. Tomogr. **18**, 110–118 (1994).
[13]S. Surti and J. S. Karp, "Imaging characteristics of a 3-dimensional GSO whole-body PET camera," J. Nucl. Med. **45**, 1040–1049 (2004).
[14]J. S. Kim *et al.*, "Performance measurement of the microPET Focus 120 scanner," J. Nucl. Med. **48**, 1527–1535 (2007).
[15]National Manufacturers Association, "Performance measurements of small animal positron emission tomographs," NEMA Standards Publication No. NU 2-2008 (National Electrical Manufacturers, Washington, DC, 2008).
[16]Y. C. Tai *et al.*, "Performance evaluation of the microPET Focus: A third-generation microPET scanner dedicated to animal imaging," J. Nucl. Med. **46**, 455–463 (2005).
[17]C. C. Watson, "New, faster, image-based scatter correction for 3D PET," IEEE Trans. Nucl. Sci. **47**, 1587–1594 (2000).
[18]M. Lubberink, S. A. van, H. W. de Jong, G. A. van Dongen, and G. J. Teule, "Acquisition settings for PET of 124I administered simultaneously with therapeutic amounts of 131I," J. Nucl. Med. **47**, 1375–1381 (2006).

Interior SPECT Reconstruction Problem with Tiny *a proiri* Knowledge – An Application for High Resolution Pinhole Brain Imaging

Qiu Huang, Tsutomu Zeniya, Hiroyuki Kudo, Hidehiro Iida, and Grant T. Gullberg

***Abstract*— The quantitation of cerebral blood flow (CBF) and cerebral vascular reactivity (CVR) are valuable in diagnosing brain ischemia, and the quantitation of benzodiazepine receptor density is important in evaluating neuronal damage due to ischemic effects. To better evaluate cerebral autoregulation, a high resolution brain single photon emission computed tomography (SPECT) imager is being built that provides an image of the entire brain for support information in the reconstruction of the interior problem from small field-of-view, truncated projections for high resolution ROI imaging.**

Kudo *et al.* presented a unique and stable solution to the interior problem in computed tomography (CT) given tiny *a proiri* knowledge of the object. In this work we advance their result to the interior reconstruction problem in SPECT where a uniform attenuation map is assumed in brain imaging.

In the theory, differentiation followed by backprojection (DBP) of truncated SPECT data is shown to obtain the truncated weighted Hilbert transform. Then with *a proiri* information on a small part of the region-of-interest (ROI), the other part of the ROI is shown to be available using the projection onto convex sets (PCOS) method. Simulations show that the algorithm provides quantitative results for the reconstruction of the fan-beam tomographic data. Iterative reconstruction of the pinhole data is under investigation to verify the accuracy of the central slice and to provide reasonable results for regions off the central slice.

***Index Terms*—interior problem, SPECT, uniform attenuation, brain imaging.**

I. Introduction

The Department of Investigative Radiology at the National Cardiovascular Center Research Institute in Osaka, Japan is designing a high resolution single photon emission computed tomography (SPECT) imager for obtaining high resolution brain scans for various imaging diagnostic applications. The camera consists of one large field of view detector imaging the whole brain and multiple smaller field of view high resolution detectors imaging small regions of the brain (see Fig. 1). The large field of view detector provides images without truncation that localize areas of particular diagnostic interest and provide support information for the reconstruction of high resolution regions of interest (ROIs) from high resolution truncated projections obtained with the small field of view detectors. The work presented in this paper develops an algorithm that accurately reconstructs uniformly attenuated truncated projections, which is an extension of the interior reconstruction problem for the reconstruction of non attenuated truncated projections.

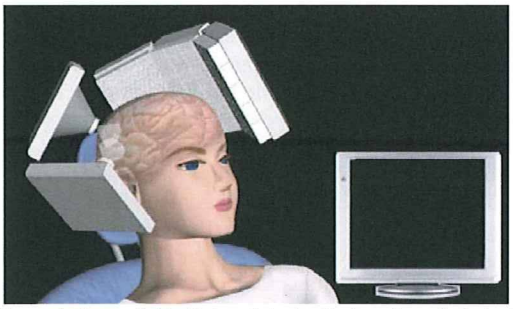

Figure 1. Large field of view detector for imaging whole brain and smaller field of view detectors for imaging ROIs.

The Department of Investigative Radiology has been involved in a large-scale multicenter clinical study aimed at evaluating validity and impact of a quantitative SPECT reconstruction package (QSPECT) [1] for multicenter clinical studies. The quantitative SPECT reconstruction package provides quantitative functional parametric images which are consistent among different setup of equipments and institutions. This allows the use of SPECT in a large scale clinical evaluation for diagnosing brain autoregulatory abnormalities. (A review of noninvasive diagnostic tests to assess cerebral autoregulation can be found in [2].) Dynamic SPECT scans are used to quantify cerebral blood flow (CBF) and cerebral vascular reactivity (CVR) in a single session using a split dose administration of ^{123}I iodo-amphetamine (IMP); one at rest and one during Diamox challenge [3]. Clinical data using QSPECT demonstrated that CBF at rest and during Diamox was reproducible among institutions.

This work was supported in part by the National Institutes of Health under Grant R01 EB00121, and in part by the Director, Office of Science, Office of Biological and Environmental Research, Medical Sciences Division of the U.S. Department of Energy under Contract DE-AC02-05CH11231.

Qiu Huang is with Lawrence Berkeley National Laboratory, One Cyclotron Road, MS 55R0121, Berkeley, CA 94720-8119. (phone: 510-495-2714; fax: 510-486-4768; e-mail: qhuang@lbl.gov).

Tsutomu Zeniya is with the National Cardiovascular Center Research Institute, Suita, Osaka, Japan (e-mail: zeniya @ri.ncvc.go.jp).

Hiroyuki Kudo is with University of Tsukuba, Tsukuba, Japan (e-mail: kudo@*is*.tsukuba.ac.jp).

Hidehiro Iida is with the National Cardiovascular Center Research Institute, Suita, Osaka, Japan (e-mail: iida@ri.ncvc.go.jp).

Grant T. Gullberg is with Lawrence Berkeley National Laboratory, One Cyclotron Road, MS 55R0121, Berkeley, CA 94720-8119. (e-mail: gtgullberg@lbl.gov).

Another important part of the multi-center trial is to evaluate neuronal damage due to ischemia and to provide prognostic value for surgical outcomes. Damage of benzodiazepine receptors has been found in cases of patients with severe brain ischemia [4]. Also, alterations of central benzodiazepine receptors have been described in several neuropsychiatric conditions, including epilepsy, Alzheimer's disease, Huntington's chorea and schizophrenia. Carbon-11-flumazenil, a benzodiazepine antagonist, has been used as a PET radiotracer for visualization and quantification of benzodiazepine receptors in humans. Recently, an iodinated analog of flumazenil, iomazenil has been introduced as a SPECT radiotracer. SPECT imaging of iodine-123-iomazenil (Iomazenil) binding to benzodiazepine receptors in the brain is being used to evaluate neuronal damage caused by ischemia [4] and the prognosis prior to carotid endoarterectomy [5]. Kinetic model-based methods have been developed for SPECT to quantitatively measure ^{123}I-iomazenil binding to benzodiazepine receptors in the human brain [6].

The Department of Investigative Radiology is developing a camera that will perform high resolution imaging of local ROIs in the brain to better address these imaging applications. Imaging with a high resolution small field of view camera provides truncated projections. The reconstruction of these projections involves determining the solution to the interior problem in local tomography. The interior problem in medical imaging refers to the situation where the region-of-interest (ROI) is totally contained within the object. For instance, in SPECT, the interior problem happens when the projections passing through the region outside the ROI are truncated due to a small field-of-view detector or a short detector-to-object distance in the case of converging collimation. The interior problem has been studied for some time [7]. Recently, Kudo *et al.* [8] proved that the solution is unique and stable in computed tomography (CT) if a small region in the ROI is known *a proiri*. In this paper this result is extended to the SPECT interior reconstruction problem.

Both in the work of Kudo *et al.* and in the work presented in this paper, the theory for the solution to the interior problem is based on the differentiation backprojection (DBP) method. The concept of DBP was first developed in parallel beam [9] and cone-beam [10] geometry in CT. The non interior truncation problem was solved for CT in [11], [12], [13], [14], [15]. Similar works in SPECT can be found in [16], [17], [18], [19], [20], where uniform attenuation was assumed. In SPECT the assumption of uniform attenuation is reasonable for some applications such as in brain imaging [21]. The result of the work in this paper shows that, with *a proiri* information of the ROI, the brain image can be reconstructed even when the imaging geometry forms an interior problem. It is expected that this result is useful in the reconstruction of pinhole data, where a pinhole collimator is attached to the small field-of-view cameras for imaging the brain. The pinhole collimator provides a small field-of-view (FOV) with high sensitivity and high resolution when located close to the object.

The paper is organized as follows: Section II shows that the differentiated backprojection (DBP) of fan-beam data is related to the distribution of the radioactive tracer in SPECT through a truncated weighted Hilbert transform. Then a unique inversion is shown to exist for the truncated weighted Hilbert transform given a small region of ROI is known *a proiri*. The results of numerical simulations are presented in Section III where the theory is shown to give a measure of confidence for the quantitative accuracy of the fan-beam reconstruction problem and the conclusion is given in Section IV.

II. Method

The method in this work is illustrated by showing that the differentiated backprojection (DBP) of fan-beam data is related to the distribution of the radioactive tracer in SPECT through a truncated weighted Hilbert transform and the truncated weighted Hilbert transform can be inverted given some prior information.

A. DBP operation for fan-beam data

For a transaxial slice, let $f(x,y)$ represent the distribution of the radiopharmaceutical in body tissues, which is assumed to be a smooth and compactly supported function of R^2. The SPECT image reconstruction estimates $f(x,y)$ from the detected photon counts. We denote $\vec{r}=(x,y)$ and $D=\{(x,y)\in R^2:\ x^2+y^2\le 1\}$. We assume $f(x,y)\equiv 0$ outside of D and the attenuation μ of the body tissues is uniform inside D. A typical fan-beam data acquisition geometry with a circular focal-point trajectory is shown in Fig. 2, where each projection ray is represented by (β,σ). One particular projection ray is shown emanating from the focal point S for the angle β with the ray angle σ.

In this paper, the fan-beam uniformly attenuated projection of the function $f(x,y)$ is defined as

$$[D_\mu f](\beta,\sigma)=\int_0^\infty f(S+\tau\vec{\alpha}(\beta,\sigma))e^{\mu\tau}d\tau\,, \qquad (1)$$

where $D_\mu f$ is the projection operator for the uniformly attenuated fan-beam projection data, $\sigma\in[-\sigma_m,\sigma_m]$, and $\vec{\alpha}(\beta,\sigma)$ is a unit vector in R^2 representing the direction from the focal point to the collimation hole, as shown in Fig. 2. Here, $\sigma_m\in(0,\pi/2)$ denotes the maximum angle subtended by the fan-beam. Let R be the radius of the circular focal point trajectory. We can modify the fan-beam data to obtain:

$$g(\beta,\sigma)=e^{-\mu R\cos\sigma}[D_\mu f](\beta,\sigma)\,. \qquad (2)$$

Define

$$s=R\sin\sigma,\quad \theta=\sigma+\beta$$

$$\hat{\sigma}(r,\varphi,\theta)=\arcsin\frac{\vec{r}\cdot\vec{\theta}}{R}=\arcsin\frac{r\cos(\theta-\varphi)}{R}\,.$$

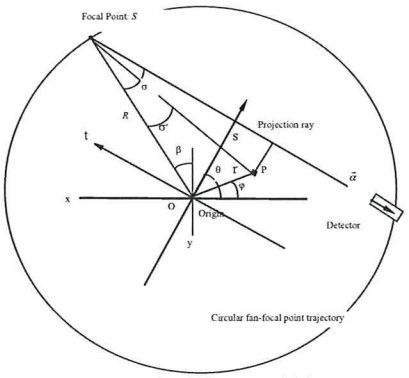

Figure 2. A typical fan-beam acquisition geometry.

We denote $\vec{\theta} = (\cos\theta, \sin\theta)$ and $\vec{\theta}^{\perp} = (-\sin\theta, \cos\theta)$ and construct an image:

$$\hat{f}(x,y) = -\frac{1}{2}\int_{-\pi/2}^{\pi/2} \frac{e^{i\vec{\sigma}\cdot\vec{\theta}^{\perp}}[(\frac{\partial}{\partial\sigma} - \frac{\partial}{\partial\beta})g](\theta - \hat{\sigma}(r,\varphi,\theta), \hat{\sigma}(r,\varphi,\theta))}{R\cos\hat{\sigma}(r,\varphi,\theta)} d\theta. \quad (3)$$

This image was proved to be related to the original distribution of radiopharmaceutical as [17]:

$$\hat{f}(x,y) = \int_{-\infty}^{\infty} \frac{\cosh(\mu\tau) f(x-\tau, y)}{\pi\tau} d\tau. \quad (4)$$

Equation (3) involves the operations of derivative and backprojection for the modified attenuated projection in fan-beam geometry and can be readily obtained from fan-beam measurements. Equation (4) shows that the image $\hat{f}(x,y)$ is an image obtained by convolving the true image with a one-dimensional (1D) kernel $\cosh(\mu t)/(\pi t)$ multiplied by some factor, thus the image reconstruction is accomplished by inverting the convolution corresponding to a truncated weighted Hilbert transform.

B. *Inversion of Truncated Hilbert Transform*

Denote the left hand side of (4) by $g(t)$ and the distribution of activity by $f(t)$. The reconstruction is to solve the following integral equation:

$$g(t) = \int_{-1}^{1} \frac{\cosh(\mu\tau) f(t-\tau)}{\pi\tau} d\tau.$$

As shown in Fig. 3, the function $f(t)$ has a support in $-1<t<1$. There is no loss of generality since shifting and scaling can always transform any support interval to $(-1,1)$.

If $g(t)$ is known for $-1<t<1$, the equation can be solved as in [19] and [17]. Unfortunately, for some geometries the function $g(t)$ is only available on a small interval $-1<a<t<d<1$. Then the algorithms in [19] and [17] do not guarantee a stable inversion. However, based on the work by Kudo et al [8], we

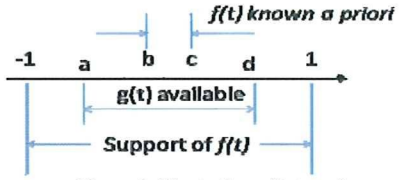

Figure 3. Illustration of intervals.

found if the value of $f(t)$ in the interval $a<b<t<c<d$ is assumed to be known, then the inversion is available in (a,d).

The reconstruction problem becomes:

$$g(t) = \int_{-1}^{1} \frac{\cosh(\mu\tau) f(t-\tau)}{\pi\tau} d\tau \quad . \quad (-1 < a < t < d < 1), \quad (5)$$

subject to $f(t) = f^{(p)}(t)$ for $(a < b < t < c < d)$.

According to [17], we know the inversion can be obtained by constructing a new function from $g(t)$:

$$\int_{-1}^{1} \frac{g(s)}{\pi(s-t)} \frac{\sqrt{1-t^2}}{\sqrt{1-s^2}} ds.$$

In this case, this function can be broken into two terms: $h_1(t) + h_2(t)$, where

$$h_1(t) = \int_{a}^{d} \frac{g(s)}{\pi(s-t)} \frac{\sqrt{1-t^2}}{\sqrt{1-s^2}} ds,$$

$$h_2(t) = \left(\int_{-1}^{a} . + \int_{d}^{1} . \right) \frac{g(s)}{\pi(s-t)} \frac{\sqrt{1-t^2}}{\sqrt{1-s^2}} ds.$$

The first term $h_1(t)$ is available from the truncated weighted Hilbert transform $g(t)$ for $a<t<d$, while the second term $h_2(t)$ remains unknown.

Since the function $f(t)$ is known for $b<t<c$, the second term in this interval can be represented as

$$h_2(t) = \left[\left((I+\Phi) f^{(p)}\right)\right](t) - h_1(t) \qquad \text{for} \qquad t \in (b,c).$$

Here, the operator Φ is the same as in [17] and I indicates the unity operator.

According to the continuity property of analytical functions, the function $h_2(t)$ can be analytically continued from the known interval (b, c) on the real axis to the larger interval (a, d) on the real axis. Since both $h_1(t)$ and $h_2(t)$ are uniquely determined for $t \in (a,d)$, function $f(t)$ is uniquely determined for $t \in (a,d)$. Then the projection onto convex sets (PCOS) method [22] was used to solve the integral equation in (5). Numerical results will be shown in the next section.

III. Numerical Results

In the fan-beam SPECT simulation study, the object image is chosen to be the modified Shepp-Logan phantom shown in Fig. 4. Uniform attenuation coefficient $\mu = 0.15 cm^{-1}$ was chosen to generate the truncated attenuated fan-beam data.

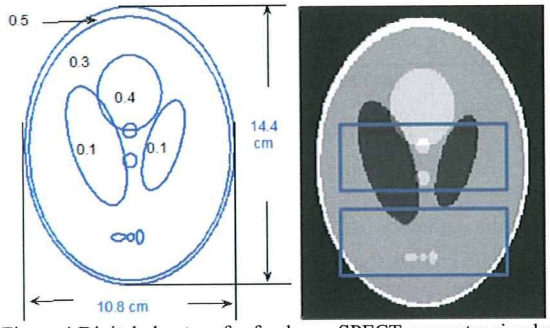

Figure 4 Digital phantom for fan-beam SPECT computer simulation. The square boxes in the right image indicate two regions-of-interest (ROIs).

In the reconstruction, first, differentiation followed by backprojection of truncated SPECT data was obtained. Then assuming the activity within a small part of the region-of-interest is known, the other part of the ROI was estimated using the PCOS method. The reconstructed image is shown in Fig. 5.

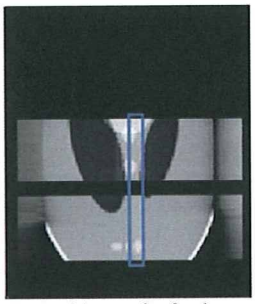

Figure 5: The reconstructed image for fan-beam geometry. The box indicates the region where the distribution is known *a priori*.

IV. Conclusion

This paper extended the work in [8] to SPECT imaging where uniform attenuation map is assumed. The interior problem was shown to be solvable given tiny *a priori* information. Reconstructions from simulated fan-beam data verify the theory.

The investigation of a pinhole system is presently undergoing. In the pinhole simulation, regularized maximum *a posteriori* (MAP) algorithm is used to reconstruct the simulated pinhole data. A low resolution reconstruction of the parallel beam collimated data is used as prior information.

References

[1] Iida H, Hayashida K, Nakazawa M and Katabuchi T, "Multicenter evaluation of quantitative SPECT reconstruction package – QSPECT & DTARG," *J. Nucl. Med.* 47 (Supplement 1), pp. 121, 2006.

[2] Rudzinski W, Swiat M, Tomaszewski M and Krejza J, "Cerebral hemodynamics and investigations of cerebral blood flow regulation," *Nucl Med Rev*, vol. 10, pp. 29-42, 2007.

[3] Imaizumi M, Kitagawa K, Hashikawa K, Oku N, Teratani T, Takasawa M, Yoshikawa T, Rishu P, Ohtsuki T, Hori M, Matsumoto M and Nishimura T, "Misery perfusion with split-dose ^{123}I-iodoamphetamine single-photon emission computed tomography in patients with carotid occlusive diseases," *Stroke*, vol. 33, pp. 2217-2223, 2002.

[4] Moriwaki H, Matsumoto M, Hashikawa K, Oku N, Ishida M, Seike Y, Fukuchi K, Hori M and Nishimura T, "Iodine-123-iomazenil and iodine-123-Iodoamphetamine SPECT in major cerebral artery occlusive disease," *J Nucl Med*, vol. 39, pp. 1348-1353, 1998.

[5] Tsuchida T, Yonekura Y, Sadato N, Takahashi N, Yamamoto K and Ishii Y, "Prediction of improvement of cerebral perfusion with I-123 iomazenil SPECT," *Annals of Nucl. Med.*, vol. 13, pp. 265-268, 1999.

[6] Dargham A, Larulle M, Seibyl J, Rattner Z, Baldwin R M, Zoghbi S S, Zea-Ponce Y, Bremner J D, Hyde T M, Charney D S, Hoffer P B and Innis R B, "SPECT measurement of benzodiazepine receptors in human brain with iodine-123-iomazenil: kinetic and equilibrium paradigms," *J. Nucl. Med.*, vol. 35, pp. 228-238, 1994.

[7] Natterer F, *The Mathematics of Computerized Tomography* (SIAM), 1986.

[8] Kudo H, Courdurier M, Noo F and Defrise M, "Tiny *a proiri* knowledge solves the interior problem in computed tomography," *Phys. Med. Bio.*, vol. 53, pp. 2207-2231, 2008.

[9] Noo F, Clackdoyle R and Pack J D, "A two-step Hilbert transform method for 2D image reconstruction," *Phys. Med. Biol.*, vol. 49, pp. 3903-3923, 2004.

[10] Zou Y and Pan X, "Exact image reconstruction on PI-lines from minimum data in helical cone-beam CT," *Phys. Med. Biol.*, vol. 49, pp. 941-959, 2004.

[11] Pack J D, Noo F and Clackdoyle R, "Cone-beam reconstruction using the backprojection of locally-filtered projections," *IEEE Trans. Med. Imag.*, vol. 24, pp. 70-85, 2005.

[12] Pack J D and Noo F, "Cone-beam reconstruction using 1D filtering along the projection of M-lines," *Phys. Med. Biol.*, vol. 49, pp. 2317-2336, 2004.

[13] Ye Y and Wang G, "Filtered backprojection formula for exact image reconstruction from cone-beam data along a general scanning curve," *Med. Phys.*, vol. 32, pp. 42-48, 2005.

[14] Zou Y and Pan X, "Image reconstruction on PI-lines by use of filtered backprojection in helical cone-beam CT," *Phys. Med. Biol.*, vol. 49, pp. 2717-2731, 2004.

[15] Zou Y and Pan X, "An extended data function and its generalized backprojection for image reconstruction in helical cone-beam CT," *Phys. Med. Biol.*, vol. 49, pp. N3837, 2004.

[16] Huang Q, You J, Zeng G L and Gullberg G T, "Exact Reconstruction From Uniformly Attenuated Helical Cone-Beam projections in SPECT," LBNL Technical Report, LBNL-1359E, Lawrence Berkeley National Lab, Berkeley, USA., 2008.

[17] Huang Q, You J, Zeng G L, and Gullberg G T, "Reconstruction from uniformly attenuated SPECT partial-scan projection data using DBH method," IEEE Trans. Med. Imag., vol. 28, pp. 17-29, 2009.

[18] Noo F and Pack J D, "Theory for image reconstruction from divergent beam projections in SPECT," *IEEE Nuclear Science Symposium Conference Record*, vol. 6, pp. 3449-3452, 2006.

[19] Noo F, Defrise F, Pack J and Clackdoyle R, "Image reconstruction from truncated data in SPECT with uniform attenuation," *Inverse Problems*, vol. 23, pp. 645-667, 2007.

[20] Rullgard H, "An explicit inversion formula for the exponential Radon transform using data from 180 degrees," (Preprint in 2002 Sep) *Ark. Math.*, vol. 42, pp. 353-362, 2004.

[21] Liang Z, Ye J and Harrington D P, "Quantitative brain SPECT in three dimensions: an analytical approach without transmission scans," *Three-Dimensional Image Reconstruction in Radiology and Nuclear Medicine*, Kluwer Academic Publishers, pp. 117-132, 1996.

[22] Youla D C and Webb H, "Image restoration by the method of convex projections: Part I. Theory," *IEEE Trans Med. Imag.*, vol. 1, pp. 81–94, 1982.


３．PET 装置ならびに関連技術の進歩

国立循環器病センター研究所　先進医工学センター　放射線医学部
越野一博　平野祥之　寺本昇　渡部浩司　飯田秀博

１．はじめに

PET (positron emission tomography)は、SPECT と並ぶ核医学的診断手法の一つで、陽電子放出核種を用いて断層撮像を行い、病態の変化や治療効果を高感度、低侵襲で観察することが可能である。PET では多種多様な放射性薬剤（トレーサー）を用いることで、トレーサーの体内における分布や動態から、血流量、酸素代謝率や酸素摂取率などの循環代謝、脂肪酸、ブドウ糖やアミノ酸に代表される基質代謝および神経伝達・受容体機能を画像化・定量評価することが可能である。本稿では、PET 装置および関連技術の進歩、そして心筋 PET の有用性と課題について紹介する。

２．PET 装置の進歩

PET 装置の基本性能の主な指標として、空間分解能、感度、最高係数率がある。トレーサー核種から放出された陽電子が体内組織の電子と対消滅を起こすと、一対のγ線が発生する。γ線を精度良く検出することは、高解像度の PET 画像が得られることにつながり、例えば FDG-PET においては、腫瘍と正常組織との判別を容易にし、診断能の向上につながる。またγ線を高感度で検出することは、少量のトレーサーによる画像診断を可能とし、被検者の被ばく低減につながる。優れた最高係数率の装置では、γ線の数え落としが少なく、偶発・散乱同時計数の影響を受けにくいため、定量精度を保証する要因となる。本節では、PET の原型となる装置(PETT)が 1975 年に Ter-Pogossian らによって発表されて以降、高空間分解能や高感度撮像を実現するために開発されてきた装置および技術について述べる[1-2]。

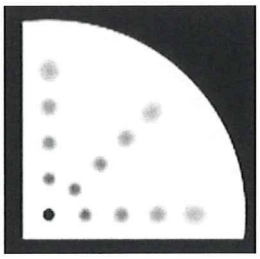

図１　辺縁部での画質低下
（シーメンス旭メディテック（株）提供）

２．１ 撮像装置

従来型 PET ではγ線検出器の厚みにより、視野辺縁部では感度分布が広がり空間分解能が低下するという問題があった（図 1)。この様な問題を解決するために DOI-PET（depth-of-interaction PET）や TOF- PET

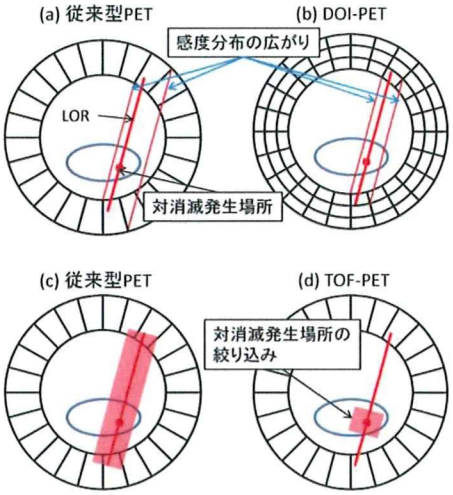

図２　従来型 PET 装置と DOI-PET および TOF-PET の概念図

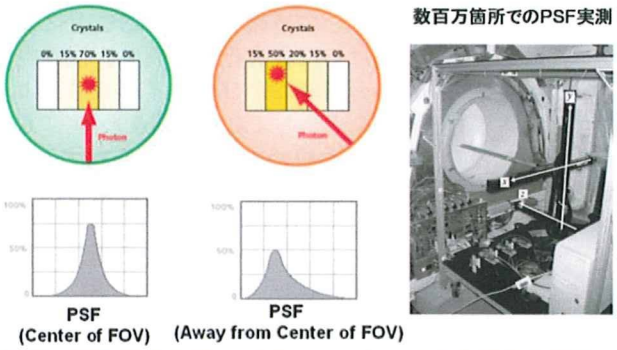

図３　PSF（Point Spread Function）による入射角の推定
（シーメンス旭メディテック（株）提供）

(time-of-flight PET)が開発されている。図２に従来型 PET と DOI-PET および TOF-PET の概念図を示した。DOI-PET では、検出器における深さ方向の相互作用位置を利用することで、感度分布の広がりを抑制し、空間分解能および感度を向上させた。PET 装置で測定される情報は電子－陽電子対消滅により発生したγ線の発生場所ではなく、一対のγ線検出器を結ぶ LOR (line-of-response)である。TOF-PET は二個の検出器にγ線が到達する時間差を利用して、LOR 上のγ線発生場所を測定し、空間分解能および感度の向上を実現している。

２．２ 画像再構成

装置の性能向上に加えて、新しい画像再構成法も提

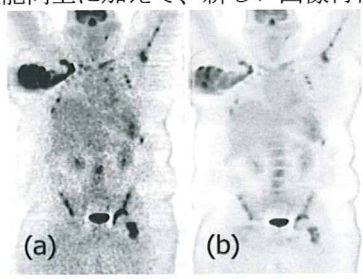

図4 HD-PETによる画像再構成 (a) PSFなし (b) PSFあり
（シーメンス旭メディテック（株）提供）

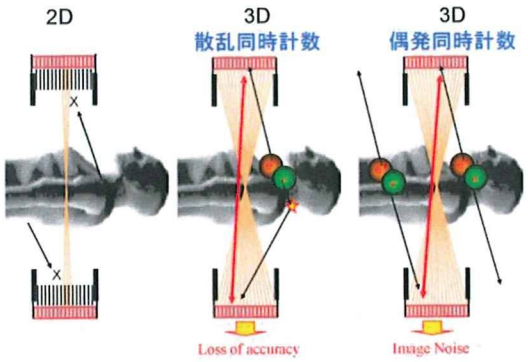

図5 2D-PETおよび3D-PETにおけるノイズの影響

案されている。その1例として、点広がり関数（PSF、point-spread-function）を用いた画像再構成法がある。図3のようにあらかじめ視野内における点広がり関数を測定し、画像再構成時にこの情報を利用することによって、視野辺縁部における画質劣化を抑制し、視野内全域における均一な高分解能および、ノイズ低減によるコントラストの向上を果たしている（図4）。他にもMRI画像などの形態情報を用いて画像再構成を行い、PET画像の空間分解能を向上させる手法も提案されている。

2．3 2D-PETおよび3D-PET

2D-PET装置は、リング間に散乱線を除去するためのセプタ構造をもち、定量性が高い反面、感度が低い。現在主流となっている3D-PETはセプタをもたず、多層のリング間での同時計数を測定するため、感度が2D収集時に比べて6〜8倍高い。PET-CT装置はほとんどが3D-PETである。感度が高い一方で、散乱線などが増加するため、定量性は2D-PETに比べて劣るといわれてきた（図5）。しかしながら3D-PETを用いた^{13}N-アンモニアや^{15}O-標識水 心筋PET検査における定量性について評価が進んでいる[3-4]。

3．心筋PETイメージング

3．1 心筋PET検査の有用性

心臓イメージングにおいては、CT angiography (CTA)を用いた冠動脈病変に関する報告が多数なされている。しかしながらCTAでは、高輝度信号として観測される石灰化プラークなどにおいて、その信号が本来の大きさを超えて近傍領域に広がって観測されるため、狭窄

重症度を過大評価することや、CTAによる形態情報に

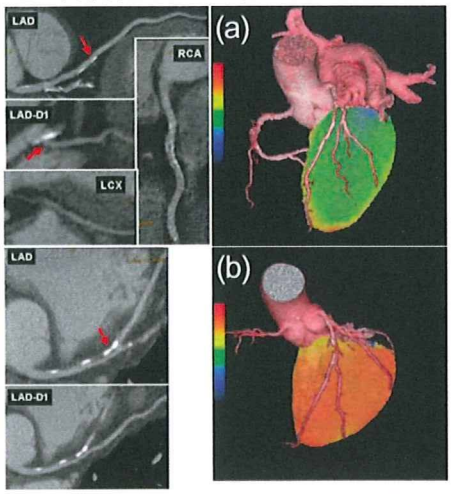

図6 動脈硬化症例における血管反応性の画像評価。
CT angiographyによる血管形態画像と^{15}O-標識水PETによる心筋灌流画像の融合。共に狭窄が認められるが、(a) 血流予備能が低下している例 (b) 血管予備能が保たれている例
（Finland, Truku PETセンター Knuuti教授提供）

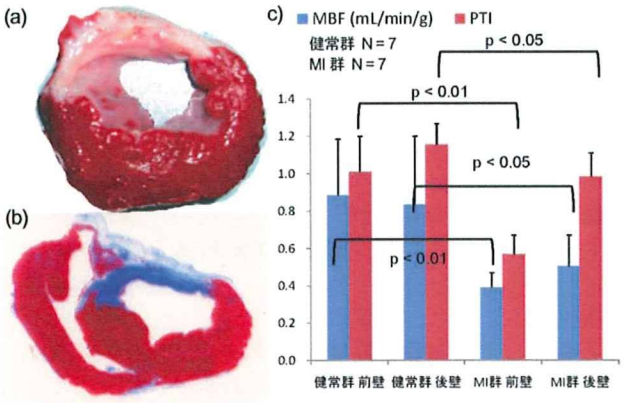

図7 家畜ブタを対象とした^{15}O-標識水PET (a) Macro (b) Histology (c) 心筋血流量 (MBF) とPTI値に関する比較

基づく予測と、PETやSPECTなど生理学的情報による心筋虚血診断との乖離が指摘されている[5]。Knuutiらは、CTモダリティの高空間分解能という利点を生かした血管形態画像と、^{15}O-標識水PETによる心筋灌流画像を図6のように三次元的に融合し、その有用性を報告している[6]。図6は、CTAでは共に狭窄を有する症例であるが、^{15}O-標識水PETによって得られた心筋血流予備能が顕著に異なっている例である。心筋虚血の指標の一つである血流予備能には、狭窄以外の微少循環に関わる因子が関与していると考えられている。循環器病疾患の予防や治療の客観的評価を可能とする微小血管の機能と構築に関する診断法の確立が期待されている。^{15}O-標識水PETでは、心筋血流量や血流予備能の他に、灌流可能な心筋組織すなわち微小循環に関する評価が可能である。

我々のグループが家畜ブタ心筋梗塞モデルを対象に行った^{15}O-標識水PET実験では、病態モデル群において心拍数、駆出率、拡張期圧について健常群に対する有意な低下が認められた。PET解析では、梗塞（前壁）

領域だけでなく、対側（後壁）領域においても組織血流量（MBF）と灌流可能な心筋組織の割合（PTI）の有意な低下が認められた（図７）。病理組織学的所見では、対側領域の心壁肥厚の他、心筋組織の線維化が観察された。対側領域における PTI の低下は、そのような現象を反映していると考えている。PTI に関しては、値 0.7 をカットオフとする、viable と non-viable な組織の判別の可能性が示唆されている[7-9]。現在、我々のグループでは、家畜ブタおよびミニブタ心筋梗塞モデルを対象とした心筋シート移植再生医療において、PTI のサロゲートマーカーとしての有用性を検証中である。

PET との一体型装置として、PET-MRI 装置の開発も進んでいる[1)、10)]。MRI は CT よりも軟組織の描出に優れており、詳細な形態情報に基づく心機能（拍出量、駆出率、心壁厚変化など）や冠動脈狭窄評価に適したモダリティである。一体型 PET-MRI 装置では、PET-CT 装置と比較しての被ばく量低減、PET および MRI の同時撮像による検査時間の短縮化に加えて、生理学的機能評価と形態・運動機能評価の融合による循環器病疾患の本態解明が進むと期待されている。

3. ２心筋イメージングの課題

PET は、1) SPECT と比較して 100 倍以上の高い感度、2) 高空間分解能、3) 虚血診断およびバイアビリティに対する高い診断精度（感度・特異度）、3) 多様なトレーサーが利用可能、という特徴を有し、心筋イメージングにおける優れたモダリティの一つである。しかしながら、全国の PET 装置普及台数は SPECT 装置の 1/10 以下である。PET 装置の普及を妨げている要因としては、装置自体のコストの他に、トレーサー合成や定量精度において、1) 施設外供給可能なトレーサーが ^{18}F-FDG のみ、2) その他のトレーサーに関しては、短い放射性半減期を原因とする院内サイクロトロンの設置、あるいはジェネレーターの製造および供給体制の整備、3) 3D-PET または PET-CT 装置における定量性の検証、4) 定量解析手法の標準化、という問題や課題がある。本稿で紹介した ^{15}O 標識水心筋 PET は、正確な血流定量が可能であるが、上述した課題が残されている。心筋 PET が普及する必要条件として、トレーサー合成の観点からは、高い extraction fraction および残存細胞に依存した再分布を備えた ^{18}F 標識トレーサーあるいは ^{15}O 標識ガス超小型・全自動検査システムの開発が望まれる。定量化の観点からは、3D-PET における定量精度の確保、定量解析手法の標準化などがある。これらの課題を克服することで、心筋 PET イメージングの有用性はさらに高まると思われる。

4. おわりに

本稿では、PET 装置および関連技術の進歩、そして心筋 PET の有用性と課題について紹介した。心筋 PET イメージングは病態把握、医薬品の安全性・薬効評価や再生医療への応用など、今後も重要な役割を果たすと考える。

参考文献

1) Pichler BJ et al: J Nucl Med **49** : Suppl 2:5-23, 2008
2) Lecomte R: Eur J Nucl Med Mol Imaging. **36** Suppl 1:S69-85, 2009
3) Schepis T et al: J Nucl Med **48** : 783-789, 2007
4) Roelants V et al: J Nucl Cardiol **13**: 220-224, 2006
5) Di Carli MF et al: Circulation **115**:1464-1480, 2007
6) Knuuti J et al: Heart **94**:360-367, 2008
7) Yamamoto Y et al: Circulation **86**:167-178, 1992
8) de Silva R et al: Circulation **86**:1738-1742, 1992
9) Knappen et al: J Nucl Med **45**: 1299-304, 2004
10) Wehrl HF et al: Eur J Nucl Med Mol Imaging **36** Suppl 1: S56-68, 2009

Conceptual Design of High Resolution and Quantitative SPECT System for Imaging a Selected Small ROI of human brain

Tsutomu Zeniya, Yoshiyuki Hirano, Tomonori Sakimoto, Kenji Ishida, Hiroshi Watabe, *Member, IEEE*, Noboru Teramoto, Hiroyuki Kudo, *Member, IEEE*, Kotaro Minato, *Member, IEEE*, Jun Hatazawa, and Hidehiro Iida, *Member, IEEE*

Abstract– **We designed a concept of high resolution and quantitative SPECT for imaging a selected small region-of-interest (ROI) of human brain. This system is aimed at achieving high resolution less than 1 mm and being applied for imaging neurons and evaluating drug delivery system. Pinhole or cone-beam collimators are useful for high-resolution imaging of small ROI. However, when the ROI is smaller than the object, the projection data are truncated by radioisotope outside ROI. In the reconstructed image, the truncation causes the artifact and the overestimation of voxel value, which deceases quantitative accuracy of physiological functions. We are introducing the new truncation compensated 3D-OSEM (TC-3DOSEM) reconstruction method. The truncated data can be successfully reconstructed within ROI by fulfilling the condition that ROI contains a priori knowledge. In addition to small field-of-view (FOV) detector, we are introducing the parallel-hole collimator attached large FOV detector covering the entire brain, to acquire the non-truncated data and provide the priori knowledge in small ROI, even if the resolution of the detector is low. For imaging with high resolution, we are using $LaBr_3(Ce)$ scintilator with optically coupled to position-sensitive photomultiplier tube (H8500, Hamamatsu, Japan) as the detector. And also, for proof of our concept, we performed preliminary experiment using pinhole SPECT and brain phantom. The reconstruction ROI contained the region outside the brain, that is, zero count as the priori knowledge. The truncated data were reconstructed by TC-3DOSEM. The reconstructed image without artifact and overestimation was obtained with high resolution. This preliminary experiment suggested feasibility of high resolution and quantitative SPECT for imaging a selected small ROI of human brain.**

Manuscript received November 13, 2009. This work was supported in part by the Grant-in-Aid for Scientific Research (C) (20500435) of the Ministry of Education, Culture, Sports and Technology (MEXT), Japan, the Grant for Translational Research from the Ministry of Health, Labour and Welfare (MHLW), Japan, Newly Adopted Projects of Regional R&D Programs for FY2008 from Kansai Bureau of Economy, Trade and Industry, Japan.

T. Zeniya, Y. Hirano, K. Ishida, H. Watabe, N. Teramoto and H. Iida are with the Department of Investigative Radiology, Advanced Medical Engineering Center, National Cardiovascular Center Research Institute, 5-7-1 Fujishirodai, Suita, Osaka 565-8565 Japan (e-mail: zeniya @ri.ncvc.go.jp).

T. Sakimoto and K. Minato with the Graduate School of Information Science, Nara Institute of Science and Technology, Japan.

H. Kudo is with the Department of Computer Science, Graduate School of Systems and Information Engineering, University of Tsukuba, Japan.

J. Hatazawa is with the Department of Nuclear Medicine and Tracer Kinetics, Osaka University Graduate School of Medicine, Japan.

I. Introduction

We designed a concept of high resolution and quantitative SPECT for imaging a selected small region-of-interest (ROI) of human brain. This system is aimed at achieving high resolution less than 1 mm and being applied for imaging neurons and evaluating drug delivery system. Also, for proof of our concept, we carried out preliminary experiment using pinhole SPECT and brain phantom.

II. Conceptual Design

Pinhole or cone-beam collimators are useful for high-resolution imaging of small ROI. However, as shown in Fig. 1, when the reconstruction ROI is smaller than the object like human brain, the projection data are truncated by radioisotope outside ROI. Because of this truncation, the voxel value of the reconstructed image is overestimated. This hampers quantitative assessment of physiological functions.

Recently, Kudo et al proposed reconstruction theory to solve the interior problem in computed tomography (CT) [1]. We are applying it for pinhole and cone-beam SPECT. Let's explain how to realize with Fig. 2. According to Kudo's theory, the truncated data can be successfully reconstructed within ROI by fulfilling the condition that ROI contains a priori knowledge. In addition to small field-of-view (FOV) detector for imaging with high resolution, we are introducing the parallel-hole collimator attached large FOV detector covering the entire brain to acquire the non-truncated data, even if the resolution of the detector is low. As another condition, the reconstruction matrix must be larger than the object.

Figure 3 is a conceptual illustration of high resolution and quantitative SPECT system for imaging a selected small ROI of human brain. This system has two types of detectors. One is pinhole or cone-beam collimator attached $LaBr_3(Ce)$ scintillator with high intrinsic spatial resolution of approximately 1 mm [2] for imaging a selected small ROI with high resolution. The other is parallel-hole collimator attached NaI(Tl) scintillator with active area of 250 mm×150 mm for acquiring the non-truncated data. Position-sensitive photomultiplier tubes (H8500, Hamamatsu, Japan) are optically coupled to both scintilators.

9781-4244-3962-1/09/$25.00 ©2009 IEEE

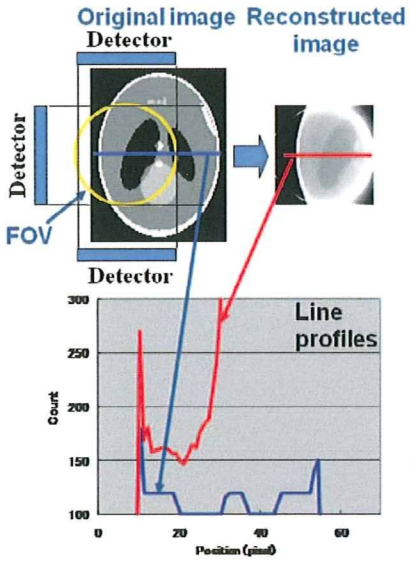

Fig. 1. The artifact and overestimation on the reconstructed image due to truncation.

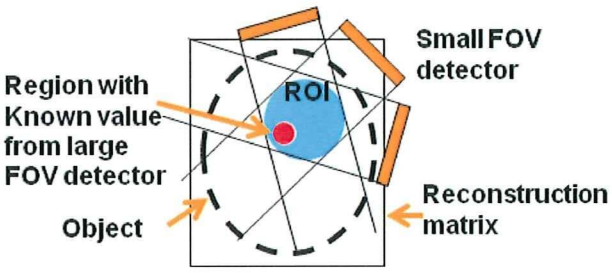

Fig. 2. Schematic diagram showing the solution of the interior problem.

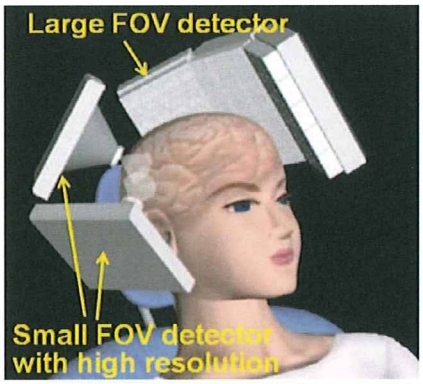

Fig. 3. Conceptual illustration of high resolution and quantitative SPECT system for imaging a selected small ROI of human brain.

III. Preliminary Experiment

For proof of our concept, we performed preliminary experiment using pinhole SPECT and Hoffman brain phantom [3]. The reconstruction ROI contained the region outside the brain, that is, almost zero count as the priori knowledge [4]. The truncated data were reconstructed by truncation compensated 3D-OSEM (TC-3DOSEM) reconstruction method for pinhole SPECT [5].

Figure 4 shows the experimental setup. We scanned a part of Hoffman brain phantom using the rotating stage and 1-mm pinhole collimator fitted to clinical SPECT gamma camera (GCA7200A, Toshiba, Japan). As for the scan parameters, the phantom was filled with Tc-99m of 1,480 MBq and scanned for 2 hours, the radius of rotation was 95mm, the imaging FOV was 95 mm, and the rotation angle was 180 degrees. This radius of rotation is that collimator doesn't hit again the phantom in case of circular orbit and 180 degrees rotation. And also, we scanned same phantom using parallel collimator to compare in terms of spatial resolution.

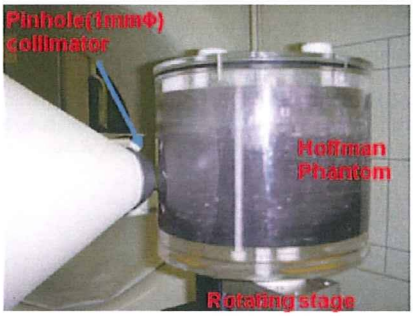

Fig. 4. Experimental setup for scanning Hoffman brain phantom by pinhole SPECT.

Figure 5 shows results of human brain phantom study. In case of clinical SPECT with parallel collimator, the resolution of the reconstructed image was low. In case of pinhole collimator and conventional 3DOSEM, the resolution was high, but the artifact appeared at the edge of ROI and the voxel counts were overestimated. On the other hand, combination of pinhole collimator and TC-3DOSEM provide high resolution image and eliminated the artifact and the overestimation. In this experimental geometry using pinhole collimator, theoretical resolution was approximately 2 mm.

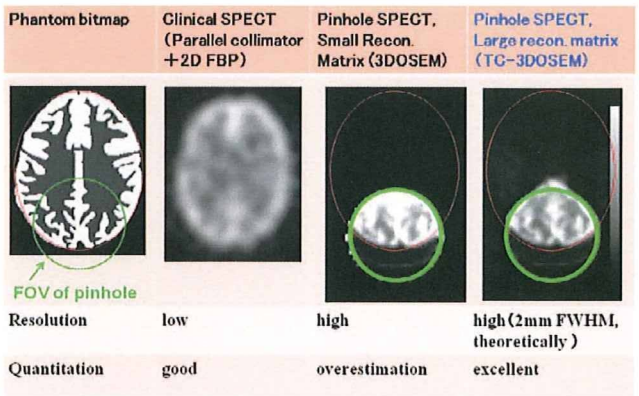

Fig. 5. Comparison of the reconstructed image from preliminary experiment using brain phantom.

IV. Conclusion

We have designed the concept of high resolution and quantitative SPECT for imaging a selected small ROI of human brain. And also, the preliminary experiment suggested

feasibility of high resolution and quantitative SPECT for human brain.

REFERENCES

[1] H. Kudo, M. Courdurier, F. Noo, and M. Defrise, "Tiny a prior knowledge solves the interior problem in computed tomography," *Phys. Med. Biol.*, vol. 53, no. 9, pp. 2207-2231, 2008.

[2] R. Pani, R. Pellegrini, M. N. Cinti, P. Bennati, M. Betti *et al.*, "$LaBr_3$:Ce crystal: The latest advance for scintillation cameras," *Nucl Instrum Meth A.*, vol. 572, pp. 268-269, 2007.

[3] E. J. Hoffman, P. D. Cutler, W. M. Digby, and J. C. Mazziotta, "3D phantom to simulate cerebral blood flow and metabolic images for PET," *IEEE Trans. Nucl. Sci.*, vol. 37, pp. 616-620, 1990.

[4] M. Defrise, F. Noo, R. Clackdoyle, and H. Kudo, "Truncated Hilbert transform and image reconstruction from limited tomographic data," *Inverse Problems*, vol. 22, pp. 1037-1053, 2006.

[5] T. Zeniya, H. Watabe, A. Sohlberg, T. Inomata, H. Kudo, et al., "3D-OSEM reconstruction from truncated data in pinhole SPECT," *2007 IEEE Nuclear Science Symposium Conference Record*, vol. 6, pp. 4205-4207, 2007.

平成19年度　ワーキンググループ報告

SPECT画像再構成・画像処理の標準化とその評価に関する研究

代表：飯田　秀博（国立循環器病センター研究所）

核医学第46巻第2号別刷
(2009年6月発行)

SPECT画像再構成・画像処理の標準化とその評価に関する研究

代表：飯田　秀博（国立循環器病センター研究所）

メンバー：
中川原譲二（中村記念病院）
松田　博史（埼玉医科大学）
中島　　孝（国立病院機構新潟病院）
石田　良雄（国立循環器病センター放射線診療部）
宮本　　享（国立循環器病センター脳神経外科）
銭谷　　勉（奈良先端科学技術大学院大学）
黒川　　徹（周東総合病院）
赤松　哲哉（アルファシステムズ株式会社）
山田　章吾（東北大学）
丸野　廣大（虎の門病院）
畑澤　　順（大阪大学）
福島　和人（国立循環器病センター放射線診療部）
橋川　一雄（国立病院機構大阪南医療センター）
鈴木　倫保（山口大学）
中澤　真弓（日本メジフィジックス株式会社）
石田　健二（株式会社モレキュラーイメージングラボ）
（現在所属　宮本　享：京都大学，銭谷　勉：国立循環器病センター研究所）

背景と目的

SPECT検査は循環器の診断において重要な役割を担い，日常の診療に広く利用されている．脳領域においては脳組織血流量や神経受容体の結合能などの機能画像の定量評価が長く試みられたが，画像精度に限界があり，PETに劣るとされてきた．心筋領域においては，定量評価というよりは放射性薬剤集積の欠損の有無を視覚的に捉えるのみであった．これは放射線の被写体内部における吸収と散乱線の補正法が未成熟であったためである．近年，吸収と散乱線を十分に高い精度で補正する方法が確立し，脳だけでなく心筋領域でも高い精度の画像が得られることが示された．また，SPECTにおける吸収と散乱線の影響は，装置幾何学には全く依存しないことが明らかになり，吸収と散乱線に対する補正がソフトウエアで行われる限りにおいて，画像の定量精度は装置に依存しない．これは多施設検討にSPECTを利用する際に重要なことであり，PETを超えた大きな利点であると考えられる．

本ワーキンググループでは，既存のSPECT装置を使った診断において，その画像精度の大幅な向上を実現し，脳および心臓を対象とした機能画像定量評価法の，施設や装置を超えた標準化を目指した．脳領域における組織血流量と血管反応性の診断においては，その妥当性検証を試みた．心筋領域においては，PETと同様に組織血流量の定量評価が可能であることを確認し，それに基づく新しい応用領域の開拓を目指した．さらに，多施設で得られたSPECT画像を集約解析するにあたっての現実的な問題と課題を明らかにすることを目的とした．

活動の進行と成果

国立循環器病センター研究所が開発した一連のプログラムをQSPECTパッケージとして整備し，当該ワーキンググループメンバー機関を中心に国内外の協力施設に配布し，個々の機関において検討がなされた．

研究協力機関においては，まず画像の均一性評価を行った上で，予め定められたプロトコルに従って画像の妥当性を評価した．基準化された円筒プールファントムに，既知かつほぼ同一量の放射性薬剤を封入し画像の均一性と定量値再現性の

評価を行ったところ，必ずしも良好ではない装置が存在した．これはクオリティコントロール(QC)の不整備が原因であった．多くの施設においては検出器の均一性補正の不備が主な理由であったが，一部では収集パラメータ(エネルギーウインドウ)に設定の誤り，あるいは装置内の補正ソフトウエアの誤りが原因であった．画質(画像の統計ノイズ)は，理論上は装置の感度にのみ起因しており，感度と解像度の高いファンビームコリメータの画像が優れるはずであったが，実際にはQCの調整不備が主な原因となり画質に差が生じていた．施設や装置を超えて標準化された画像再構成ソフトウエアによって比較がなされたことで，初めてこの問題が明らかになったことは，重要な成果である．さらに頭部を模倣するファントムを製作し，これをもとにした標準的なQC指標を構築する必要があると考えられた．

均一性補正データの調整を行った後には，すべての施設において円筒プールファントムの画像はほぼ均一であり，ほぼ同程度(±9%)の範囲で一致した定量値(Bq/ml)が確保できた．本ソフトで得られた再構成画像はカメラ数，収集時間，回転ステップ数，機種に依存せず，正確に放射能濃度を定量評価するように設計されているが，これが実験的に確認された．頭蓋の輪郭抽出法については最終的には視覚的に確認することで，それぞれのコリメータや機種に依存しない一定の定量値が得られることが期待された．

すでに別論文で報告しているDual-Table ARG理論[1]が^{123}I-iodoamphetamine(パーヒューザミン®)の2回投与法に適用され，安静時および血管拡張時の局所脳血流量の定量評価がなされた．国立循環器病センターで検討された6例の症例ではPETと一致し，また6施設において異なる日に計測した結果は，安静時および血管拡張時で10%の程度で一致した．山口大学で行われた別の検討では，389例の検査がなされた中80例が複数回検査を受診した．このうち投薬および患者症状に変化の認められなかった7例において検討がなされたところ，画像上および脳内各領域の定量値においても変化は求められなかった．同様に異なるメーカー装置を有する関連病院においても310症例中の30例で複数回検査がなされ，変化を予想しない10症例において，脳血流量画像は安静時および負荷後もよく一致した．さらにふたつの病院間で紹介された20症例中の5例が症状変化などなかったが，実際の脳血流量画像はよく一致した．また複数の健常者群における安静時および血管拡張時の脳血流量値の計測が行われているが，現時点では有意差が認められていない．さらに，埼玉医大では，内頸動脈狭窄の認知機能への影響，かつステント術による血行再建治療がどのように認知機能の改善に貢献するかについて，詳細な検討がなされた．これらは脳循環の定量評価法が標準化されて初めて検討できることであり，当該ワーキンググループ活動の重要な成果と考えられる．

中村記念病院では^{123}I-iomazenil(ベンゾダイン®)を使った早期画像と遅延画像から，中枢性ベンゾジアゼピン受容体密度の定量評価がなされた．健常者データベースの構築において，従来の画像再構成よりも高い精度を有することが示され，一方モヤモヤ病症例においては，定性的な早期画像および遅延画像では認められないような詳細な検討が，標準化された画像ソフトウエアによって可能になった．大阪南医療センターでは，機器メーカーの提供する画像では画像精度が必ずしも保証されていない可能性を指摘した．特に自動化された頭部輪郭抽出ソフトにおいては，安定した吸収補正が実現できていないことが指摘された．

心筋組織の局所血流量計測には^{201}Tlの利用が検討され，まず臨床画像において従来画像再構成法で問題となる後下壁の偽欠損アーチファクトは除去できることが示された．イヌを用いたダイナミックSPECT計測において検証がなされた[2]．さらにブタを対象に行ったダイナミックSPECT計測では，安静時および血管拡張時の心筋血流量が一回の検査のみで定量評価できることが示唆されている．さらに，虎の門病院では，運動負荷中の局所心筋血流量の定量評価が試みられ，最大心拍

数に依存していることからこの計測方法の妥当性が示唆された．一方ラットの局所心筋血流量においても局所心筋血流量が定量評価できること，病態依存性が観察できることなどが確認された．小動物から臨床まで一貫した撮像技術と診断薬剤を使って病態観察と薬効評価ができる点はPETと同様であり，今後新しい治療薬の評価に有効に利用できると考えられた．

今後の課題

当該ワーキンググループ活動では画像ソフトウエアを統一化することで，装置を超えた標準化が現実に可能であることが明らかになった．これは多施設臨床研究を実施する際に重要な利点であり，今後具体的な事例を介した実証が必要である．このためにも，当該ソフトウエアの臨床診断ツールとしての検証とapprovalが必要である．国内ではソフトウエアの薬事承認体系が整備されておらず，学会としての活動が必要である．また，空間解像度はコリメータに依存しており，結果としてSPECTで得られる機能数値は固有空間解像度や対象臓器の形状やサイズに依存する．この補正法などの標準化についても，今後詳細な検討がなされる必要がある．

謝　辞

本ワーキンググループ活動の協力機関においては，シーメンス旭メディテック株式会社，東芝メディカルシステムズ株式会社，株式会社島津製作所，株式会社日立メディコ，ジーイー横河メディカルシステム株式会社，の各機器メーカーに技術的支援をいただきました．ここに深く感謝いたします．

付　記

本ワーキンググループでは，当該メンバーが中心となってふたつの公的研究事業が開始された．厚生労働省循環器病研究委託事業『SPECT定量化システムの精度評価と標準化に関する研究』(平成19–21年度)においては脳循環定量検査法の標準化に向けた研究，特に血行力学的脳虚血診断法の標準化と頭蓋内バイパス術の評価に関する研究が，厚生労働省科学研究費補助金医療技術実用化総合研究事業『SPECT検査の精度向上と施設間誤差のない標準的画像診断法の確立』(平成19–21年度)においては，心筋領域の定量化を含む多施設臨床研究に向けたSPECT技術の整備がなされている．現在も継続しており，当該ワーキンググループの最終成果は，これらの研究事業の最終報告書を参考にされたい．

参考文献

1) Kim KM, Watabe H, Hayashi T, Hayashida K, Katafuchi T, Enomoto N, Ogura T, Shidahara M, Takikawa S, Eberl S, Nakazawa M, Iida H: Quantitative mapping of basal and vasareactive cerebral blood flow using split-dose (123)I-iodoamphetamine and single photon emission computed tomography. *Neuroimage* 2006; 33 (4): 1126–1135.
2) Iida H, Eberl S, Kim KM, Tamura Y, Ono Y, Nakazawa M, Sohlberg A, Zeniya T, Hayashi T, Watabe H: Absolute quantitation of myocardial blood flow with ^{201}Tl and dynamic SPECT in canine: optimisation and validation of kinetic modelling. *Eur J Nucl Med Mol Imaging* 2008; 35 (5): 896–905.

3-Tesla Magnetic Resonance Angiographic Assessment of a Tissue-Engineered Small-Caliber Vascular Graft Implanted in a Rat

Masashi Yamanami,[1,2] Akihide Yamamoto,[3,4] Hidehiro Iida,[3,4] Taiji Watanabe,[1,2] Keiichi Kanda,[2] Hitoshi Yaku,[2] Yasuhide Nakayama[1]

[1] Department of Bioengineering, Advanced Biomedical Engineering Center, National Cardiovascular Center Research Institute, Osaka, Japan

[2] Department of Cardiovascular Surgery, Kyoto Prefectural University of Medicine, Kyoto, Japan

[3] Department of Investigative Radiology, Advanced Biomedical Engineering Center, National Cardiovascular Center Research Institute, Osaka, Japan

[4] Department of Medical Physics and Engineering, Division of Health Sciences, Graduate School of Medicine, Osaka University, Osaka, Japan

Received 30 January 2009; revised 4 June 2009; accepted 15 July 2009
Published online 2 October 2009 in Wiley InterScience (www.interscience.wiley.com). DOI: 10.1002/jbm.b.31501

Abstract: In the development of small-caliber vascular grafts (diameter; less than 3 mm), animal implantation studies have been mostly performed by using rat abdominal aortas, and their certain patency must evaluate with sacrificing every observation periods, which is both labor-intensive and time-consuming when performing a large number of experiments. This study is the first to demonstrate the application of 3-Tesla contrast-free time-of-flight magnetic resonance angiography (TOF-MRA) in the continuous assessment of the status of a tissue-engineered vascular graft in rat. As a model graft, a single connective tubular tissue (diameter; 1.5 mm), prepared by embedding the silicone rod (diameter; 1.5 mm) into a subcutaneous pouch of a rat for 2 weeks an *in vivo* tissue-engineering, was used. The graft was implanted in the abdominal aorta (diameter; 1.3 mm) of the rat by end-to-end anastomosis. Repeated TOF-MRA imaging of the graft obtained over a 3-month follow-up period after implantation made it possible to evaluate the patency of the graft, both simply and noninvasively. It also permitted visualization of the connected abdominal aorta and renal and common iliac arteries having smaller caliber (diameter; less than 1 mm). In addition, the degree of the stenosis or aneurysm could also be detected. 3-Tesla MRA allowed the simplified and noninvasive assessment of the status on the vascular graft, including the formation of a stenosis or aneurysm, in the same rat at different times, which will be contributing to enhance the development of tissue-engineered vascular grafts even with small caliber. © 2009 Wiley Periodicals, Inc. J Biomed Mater Res Part B: Appl Biomater 92B: 156–160, 2010

Keywords: small-caliber vascular grafts; magnetic resonance angiography; animal implantation; biotube; tissue engineering

INTRODUCTION

Small-caliber arterial substitutes are needed for cardiac and peripheral revascularization procedures. For such small artery bypass grafting procedures, autologous arterial (e.g., internal thoracic artery and radial artery) or venous (e.g., saphenous vein) grafts still remain the most ideal vascular substitutes.[1,2] However, many patients do not have a vessel suitable for use owing to the poor quality, inadequate size or length, or previous harvest of such vessels. Moreover, a second surgical procedure is required to initially obtain the necessary vessel. Vascular prostheses, such as expanded polytetrafluoroethylene (ePTFE) and poly (ethylene terephthalate) (Dacron) grafts, have been used clinically for reconstructing arteries.[3] However, small-caliber (<6 mm) arterial substitutes have generally proved inadequate largely because of the formation of thromboses and intimal hyperplasia.[4,5]

Many design criteria have been proposed for the development of functional small-caliber arterial replacement grafts.[5–11] All most of all artificial vascular grafts (inner diameter, 1.5–3.0 mm) have been employed for transplantation

Correspondence to: Y. Nakayama (e-mail: nakayama@ri.ncvc.go.jp)

to rat abdominal aortas as an *in vivo* model.[6–8] Graft patency has been evaluated during the follow-up period by angiography[8] or by direct inspection at the time of removal for histological evaluation.[6,7] However, angiography requires cannulation of the carotid artery,[8] and a midline laparotomy is needed for direct inspection.[6,7] As a consequence, these methods are complex and invasive. Therefore, it is difficult to evaluate graft patency repeatedly in the same rat. Although, graft patency has also been evaluated by palpating the femoral pulse,[7] this method is subjective and uncertain.

The current imaging systems, including fluorescence antibody method, single photon emission computed tomography (SPECT),[12] laser doppler system,[13] or high-resolution ultrasound[14] for blood flow imaging in addition to magnetic resonance angiography (MRA), are powerful tool in tissue engineering field. However, it is considered that no imaging systems except for MRA fit for evaluation of the status of implanted small-caliber vascular grafts.

In clinical practice, MRI has been used as a noninvasive evaluation method for the assessment of brain blood vessels and peripheral arteries and also been widely used in preclinical research on experimental small rodents.[15–18] The studies have typically been aimed at understanding the patho-physiological status and evaluating the efficacy/side effects of newly developed treatments, such as pharmaceutical and regenerative medicine.

Our purpose in this study was to evaluate the status of a tissue-engineered vascular graft with inner diameter of 1.5 mm, clinically, repeatedly, and noninvasively in a rat implantation model. To this end, 3-Tesla contrast-free time-of-flight magnetic resonance angiography (TOF-MRA) was applied.

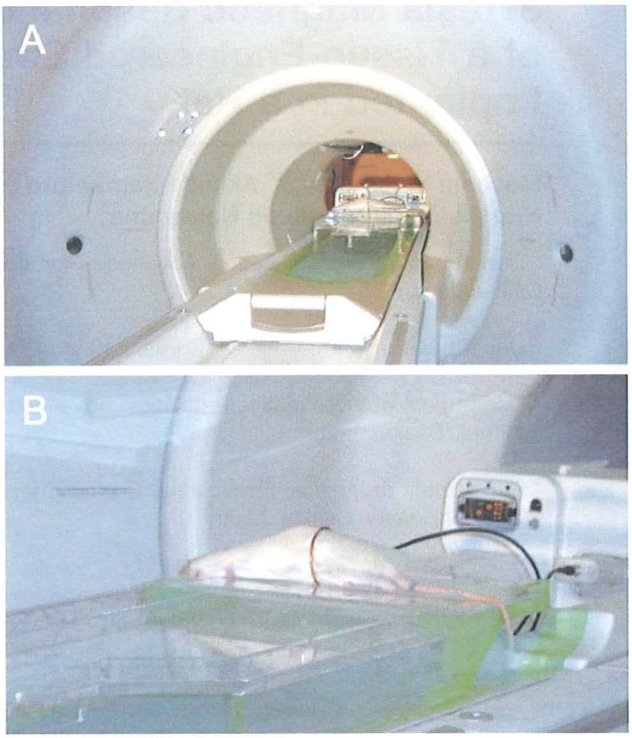

Figure 1. Experimental setup in MR imaging on a human whole-body 3T-MR scanner (GE Healthcare) (A). The coil was placed at the center of the gantry and its turn axis had perpendicular alignment to the static magnetic field (B). Rat's abdomen was positioned inside the coil along the craniocaudal direction. [Color figure can be viewed in the online issue, which is available at www.interscience.wiley.com.]

MATERIALS AND METHODS

Preparation and Implantation of the Connective Tubular Tissue

All animal experiments were conducted in accordance with local regulations, complying with the Principles of Laboratory Animal Care (formulated by the National Society for Medical Research) and the Guide for the Care and Use of Laboratory Animals (NIH Publication No. 86–23, revised 1985). The research protocol (No. 8050) was approved by the ethics committee of the National Cardiovascular Center Research Institute.

The connective tubular tissue was prepared by *in vivo* tissue engineering according to the previous reported method.[9] Briefly, a silicone rod (diameter, 1.5 mm; length, 10 mm; Tigers Polymer, Osaka, Japan) was used as a mold. One adult female Wistar rat (weight; 300 g) was anesthetized with 1.5% isoflurane (vol/vol air). The mold was placed in a dorsal subcutaneous pouch, and after 2 weeks, the implant was removed. The tubular tissue was obtained from the implant after trimming the peripheral tissues and pulling out the rod. The tube thus obtained was treated by coating with Argatroban (1 mg/graft; Mitsubishi Chemical Co., Tokyo, Japan) to make it antithrombogenic. It was then implanted to the infrarenal abdominal aorta of the same rat using an end-to-end anastomosis under microscopic guidance and sutured using 12 interrupted 10–0 nylon stitches [Figure 1(A)]. Patency was examined at the time of surgery by direct inspection. The wound was closed with 4–0 silk sutures. Thereafter, the rat had free access to standard food and water. Graft status was evaluated at 2, 36, and 78 days after transplantation by contrast-free TOF-MRA under anesthesia induced by an intramuscular injection of pentobarbital (40 mg/kg).

MR Data Acquisition

A human whole-body 3-Tesla magnetic resonance imaging (MRI) scanner (Signa, GE Healthcare, Milwaukee, WI) was employed in this study (Figure 1). The gradient coil system was capable of providing a maximum gradient amplitude of 40 mT/m. All sequence programs employed in this study were designed for clinical studies. A developed single-turn surface coil of 62 mm diameter was used for MR imaging [Figure 1(B)]. Contrast-free TOF-MRA was performed using a three-dimensional flow-compensated fast spoiled gradient recalled (3D-FSPGR) sequence [repetition

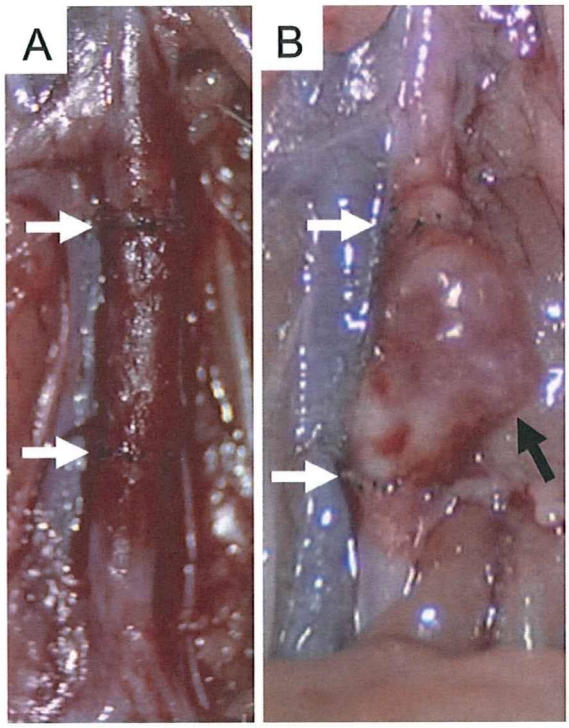

Figure 2. (A) The tubular connective tissue vascular graft (diameter; 1.5 mm) after autoimplantation in the rat infrarenal abdominal aorta (diameter; 1.3 mm) performed by end-to-end anastomosis under microscopic guidance using 12 interrupted stitches of 10-0 nylon suture. (B) The tubular connective tissue formed an aneurysm (max diameter; 3.0 mm) at 78 days after autoimplantation. White arrows indicate the proximal and distal anastomosis regions. Black arrow indicates the aneurysm. [Color figure can be viewed in the online issue, which is available at www.interscience.wiley.com.]

time (TR) = 21 ms, echo time (TE) = 5.4 ms (out of phase), flip angle (FA) = 15°, slice thickness = 0.4 mm, field of view (FOV) = 80 mm × 60 mm, matrix = 288 × 192, locs per slab = 128, the number of excitations (NEX) = 1, scanning time = 5 min 58 s]. For suppressing venous signals, a region of 40-mm thickness on the caudal side of the measured slab was saturated. The measured voxel size in TOF-MRA was 0.278 × 0.291 × 0.400 mm. The image reconstruction was zero-filled to a matrix size of 512 × 512 and the voxel size was 0.156 × 0.156 × 0.400 mm. MR angiograms were analyzed by generating the partial maximum intensity projection (pMIP) with a commercial software package (AZE, Tokyo, Japan). Our previous report on TOF-MRA was shown detail in rat.[13]

RESULTS

The tubular connective tissue with a diameter of 1.5 mm was autoimplanted successfully into the 1.3 mm diameter abdominal aorta of the rat by end-to-end anastomosis [Figure 2(A)]. After suturing with 12 interrupted stitches, there was little bleeding from either of the sites of anastomosis, indicated by the arrows in Figure 2(A). The patency of the graft was recognized directly by the satisfactory pulsation at the graft and distal side of the aorta.

3-Tesla contrast-free TOF-MRA of the rat was performed at 2 days after implantation [Figure 3(A)] to evaluate the status of the graft. The measurement time was ~6 min and no contrast medium was needed. The MRA distinctly visualized the patent graft connected to the abdominal aorta together with renal arteries and common iliac arteries of 0.7 and 0.8 mm diameter, respectively. Spatial resolution in the MRA was less than several hundred microns. A mechanical stenotic lesion, which may have been due to the anastomosis, was observed in both anastomosis regions. At 36 days after implantation, little stenosis and no aneurismal dilation of the graft were observed [Figure 3(B)]. At 78 days after implantation, the maximum diameter of the aneurysm formed at the graft was 3.0 mm [Figure 3(C)]. The shape of the aneurysm was very close to that observed macroscopically [Figure 2(B)]. Therefore, the status of the graft could be precisely determined, repeatedly, and noninvasively.

DISCUSSION

This study is the first to demonstrate the application of MRA to the evaluation of the status of a small-caliber arti-

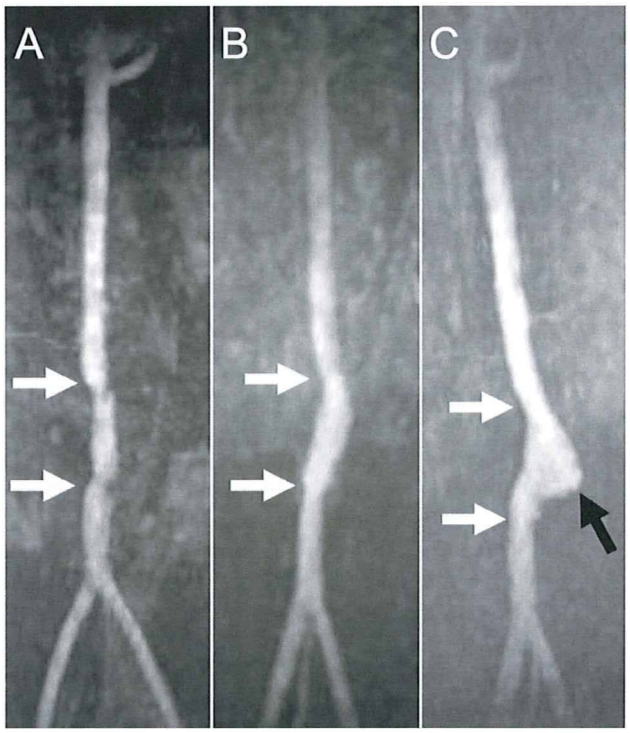

Figure 3. 3-Tesla contrast-free TOF-MRA images of the rat abdominal aorta at 2 (A), 36 (B), and 78 (C) days after autoimplantation of the biotube vascular graft. White arrows indicate the proximal and distal anastomosis regions of the abdominal aorta. A stenotic lesion was visible in the anastomosis regions at 2 days. An aneurysm formation in the graft was visible at 78 days (black arrow indicates the aneurysm).